Interannual variations in low potential vorticity water and the subtropical countercurrent in an eddy-resolving OGCM

Masami Nonaka[1]

Shang-Ping Xie[2]

and

Hideharu Sasaki[3]

[1]Research Institute for Global Change, JAMSTEC, Yokohama, Japan

[2]International Pacific Research Center and Department of Meteorology,

School of Ocean and Earth Science and Technology, University of Hawaii at Manoa,

Honolulu, Hawaii

[3]Earth Simulator Center, JAMSTEC, Yokohama, Japan

Submitted to *the Journal of Oceanography*

as a *short contribution*

Corresponding author address:
Masami Nonaka
Research Institute for Global Change,
Japan Agency for Marine-Earth Science and Technology (JAMSTEC),
3173-25 Showa-machi, Kanazawa-ku, Yokohama, 236-0001 Japan
nona@jamstec.go.jp

Abstract

Interannual-to-decadal variations in the subtropical countercurrent (STCC) and low-potential vorticity (PV) water and their relations in the North Pacific Ocean are investigated based on a 60-year-long hindcast integration of an eddy-resolving ocean general circulation model. The interdecadal intensification of STCC is associated with negative PV anomalies to the north on isopycnals beneath, by contrast, on interannual time scales, vertically coherent variations are dominant for STCC variability. This study focuses on the vertical shear of STCC in the near surface layer in relation to low-PV water in interannual variations. A correlation analysis shows that an intensified STCC vertical shear accompanies lower PV than usual to the north on 25.5 to 26.1 σ_θ isopycnal surfaces, and intensified meridional density gradient in subsurface layers. The low PV signals appear at least two years before peaks of STCC, propagating southwestward from the subduction region. These results strongly suggest that interannual to decadal variations in STCC vertical shear are associated with variations in low-PV water ventilation. Although interannual variations in STCC have been considered to relate to local wind variations, the relationship between STCC and low-PV water originally suggested by Kubokawa (1999) and found in observed climatology holds in interannual to interdecadal variations at least in this particular model.

1. Introduction

In the late1960s, a weak eastward current embedded in the broad westward current in the southern part of the North Pacific subtropical gyre was discovered (Uda and Hasunuma 1969). As its direction is opposite to that expected from the gyre circulation, it is named as the subtropical countercurrent (STCC). Although its whole distributions had not been clarified for a long time due to high eddy activity in the region (Qiu 1999), on the accumulation of observational data allowed its detailed distributions described recently (Kobashi and Kawamura 2001, 2002; Kobashi et al., 2006). Although STCC is not a strong current, the associated temperature front, the subtropical front (STF), can influence atmospheric fields aloft (Kobashi et al., 2008; Kobashi and Xie 2011). Coupled model results suggest positive coupled feedback associated with the atmospheric response (Xie et al., 2011). In coupled model projections, changes in STCC under global warming can affect significantly distributions of sea surface temperature (SST) changes in the North Pacific (Xie et al., 2010).

Formation mechanisms for STCC have been debated since its discovery. Yoshida and Kidokoro (1967) and Roden (1975) discuss possible importance of detailed distributions of zonal wind-stress, and meridional Ekman convergence, respectively. Based on ocean general circulation model (OGCM) experiments, Takeuchi (1984), however, shows that STCC can be formed without narrow scale structures in zonal wind and meridional Ekman convergence. In a theoretical study, Kubokawa (1999) proposes that STCC is associated with meridional density gradient caused by the accumulation of low-potential vorticity (PV), thick water layers subducted to the north. A numerical simulation supports this hypothesis (Kubokawa and Inui 1999). Specifically, the mode water pushes the upper pycnocline upward. On the southern flank of the mode water, this creates a northward shoaling of the upper pycnocline, which sustains an eastward current shear by thermal wind. Observational data also suggest relative distributions between STCC and low-PV water are consistent with Kubokawa’s (1999) hypothesis (Aoki et al., 2002). Further, from detailed investigation of historical observed data, Kobashi et al. (2006) show that the northern and eastern branches of STCC locate at the southern edge of the low-PV regions corresponding to the North Pacific Subtropical Mode Water (NPSMW, Masuzawa 1969; Hanawa and Talley 2001), and to the North Pacific Central Mode Water (NPCMW, Nakamura 1996; Suga et al., 1997; Oka and Suga 2006), respectively.

Although these observed climatological fields strongly support Kubokawa's (1999) hypothesis, it is still not clear if interannual to decadal variations in STCC are caused by variations of low-PV waters. On decadal time scales, in a 300-year simulation of a coupled model, Xie et al. (2011) show that STCC variations are caused by changes in low-PV water subduction. Although the resolution of the coupled model is limited and low-PV water tends to be exaggerated in the model, based on an eddy-resolving OGCM simulation Yamanaka et al. (2008) show that decadal differences in STCC are associated with those in low-PV waters, consistent with Kubokawa's hypothesis. On interannual time scales, Qiu and Chen (2010) and Kobashi and Xie (2011) indicate importance of Ekman convergence for STF and STCC, but the possibility of contribution of low-PV water variations has not been explored. The present study investigates if variations in low-PV water subduction can affect STCC on interannual time scales, based on an eddy-resolving OGCM simulation that is different from Yamanaka et al.'s

In section 2, we introduce the model and describe simulated low-PV waters. Simulated STCC is described in section 3, and relationship between interannual to decadal variations in STCC and low-PV waters is investigated in section 4. Section 5 gives summary and discussion.

2. Model

2-1. OFES

We used the Modular Ocean Model 3 (MOM3) OGCM (Pacanowski and Griffies, 2000) with substantial modification for the vector-parallel hardware system of Japan's Earth Simulator. Our ocean model for the Earth Simulator (OFES; Masumoto et al., 2004) covers a near-global domain of 75°N–75°S, with a horizontal resolution of 0.1°. The model has 54 vertical levels with resolutions of 5 m at the surface, and the maximum depth is 6065 m. For horizontal mixing of momentum and tracers, we adopted scale-selective damping with a bi-harmonic operator (Smith et al., 2000). The nonlocal K-profile parameterization (KPP) boundary layer mixing scheme (Large et al., 1994) was adopted for the vertical mixing.

The surface heat flux and evaporation were calculated by the bulk formula with atmospheric variables based on National Centers for Environmental Prediction/National Center for Atmospheric Research (NCEP/NCAR) reanalysis data (Kalnay et al., 1996) and the simulated SST field. The freshwater flux was evaluated from the evaporation field and daily precipitation rate data, under the constraint that sea surface salinity (SSS) is restored to the observed monthly climatology at a timescale of 6 days. For details, see Masumoto et al. (2004) and Sasaki et al. (2008).

Following a 50-year integration with climatological monthly-mean forcing from the annual-mean temperature and salinity climatological fields without motion, we conducted a 60-year hindcast integration with daily mean atmospheric fields of the NCEP/NCAR reanalysis data from 1950 to 2009. This hindcast simulation successfully captures variability with intraseasonal-to-decadal timescales (Sasaki et al., 2008) and has been used to investigate interannual-to-decadal variability in the western North Pacific region (Nonaka et al., 2006, 2008; Taguchi et al., 2007, 2010). In the following analyses, the resolution of our model output is reduced to 0.5° resolution for analytical convenience by selecting the data at every five grid points both in the zonal and meridional directions.

2-2. Simulated low-PV water distributions

In the present study, we investigate relationship in interannual variations between low-PV waters and STCC based on the OFES hindcast integration. Then, first we describe simulated summertime low-PV water distributions based on meridional and zonal sections of PV (Fig. 1). In the western part of the North Pacific basin, at 150°E, low-PV water corresponding to the North Pacific Subtropical Mode Water is found around 25.2-25.6 σ_θ (Fig. 1d), and its distribution is well represented in the model (Fig. 1a). In the central part of the basin in the 170°E meridional transect, low-PV water with density around 25.5 σ_θ develops more strongly in the model (Fig. 1b) than in observations (Fig. 1e), although there is PV minimum in the observation around 30°N. In the zonal section of PV at 28°N, it is confirmed that the simulated low-PV water on 26.0 σ_θ is displaced eastward compared to observations (Fig. 1c, f). Also, in the central to the eastern part of the basin, the simulated low-PV water is isolated from the lower low-PV layer by relatively high-PV water of around 26.5 σ_θ. Although the simulated low-PV water develops more strongly than the counterpart in the observation in the central to the eastern part of the basin, PV distributions are well represented to the west of the international dateline. On isopycnal surfaces (figures not shown but suggested in Fig. 5), it is confirmed that the simulated PV minimum exists about 10° longitude eastward of the observed one in layers of 25.6 σ_θ or higher density (e.g., Fig. 9 of Kobashi et al., 2006), although it is well represented in the shallower layers.

Distributions of the simulated late winter (February-March) mixed layer (ML) depth and sea surface density (Fig. 2) indicate that the deep ML develops in the western and central part of the basin to form a sharp frontal structure of ML depth. The ML depth front is somewhat sharper than in the observations (Suga et al., 2004). The sharp ML front intersects outcrop lines of around 25.5 σ_θ layers, and induces subduction of the aforementioned lower PV water in the model, as the intersection of the ML front and outcrop line is a source of low-PV water on the isopycnal layer, and a deeper ML at the intersection can induce lower PV (Inui et al., 1999; Kubokawa and Inui 1999; Xie et al., 2000).

3. Simulated STCC

3-1. Mean STCC

Fig. 3 shows the long-term mean summertime subsurface zonal current velocity field as it has a maximum in summer (not shown), consistent with observations in the eastern part of STCC (White et al., 1978; Kobashi and Kawamura 2002). STCC appears as a weak eastward flow extending in a southwest-northeast direction from 25°N, 150°E to 30°N, 170°W. At the northeastern end, STCC merges with a broad eastward flow corresponding to the northern part of the anti-cyclonic subtropical gyre. There is another strong eastward current at 19°N west of Hawaii, the Hawaiian Lee Counter Current (HLCC, Qiu et al., 1997; Xie et al., 2001), but the aforementioned STCC clearly separates from it. The simulated STCC is limited to the east of 150°E, and the northern STCC that extends in the western basin in observation (Kobashi et al. 2006) is not represented in the model. The latitude-depth section of zonal velocity around the international dateline (Fig. 3b) indicates that STCC extends from the surface to less than 200-m depth and has a vertical maximum just below the surface.

3-2. Relation between low-PV water and STCC in long-term mean and interdecadal variations

We next investigate summertime STCC and low-PV water around 170°E (Fig. 4), focusing on the eastern STCC as the western northern STCC is not represented in the model. In the latitude-depth section of long-term mean summertime PV field, there is low-PV water in the northern part of the subtropical gyre, extending southward along isopycnal surfaces around 25.3 to 25.7 σ_θ. Above the southern edge of the low-PV water (Fig. 4a), the upper pycnocline shoals northward, and STCC forms just below the sea surface (Fig. 4b). The relative position of STCC to the low-PV water is consistent with observational data (e.g., Kobashi et al., 2006), and Kubokawa's (1999) theory. To the south of STCC, there is the broad and deep westward North Equatorial Current (NEC), the southern branch of the subtropical gyre. Surrounded by the westward current of NEC, HLCC exists just to the south of 20°N. While it is also trapped in the upper layer as STCC, no low-PV water is found in the lower layer to the north of HLCC.

Horizontal distributions of layer thickness (Fig. 5) show that the maximum thickness corresponding to low-PV water appears in the western part of the basin in upper layers (Fig. 5a, b) and in the eastern/northeastern region in deeper layers (Fig. 5 b-e). The thick, low-PV water extends southeastward from its maximum and then southwestward, but directions of low-PV water ventilation are different among the layers. As a result, thick waters accumulate to the north of STCC (Fig. 5f), as suggested theoretically by Kubokawa (1999), and meridional gradient of the layer thickness from 25.1 to 26.1 σ_θ shows a local maximum almost along STCC around 27°N (Fig. 5g). In contrast, in the shallower layers (from 25.1 to 24.0 σ_θ), meridional thickness gradient is small (Fig. 5h) below STCC, indicating that the northward shoaling isopycnal surfaces in the upper layer and the corresponding eastward flow (STCC) is associated with the meridional thickness gradient of the layer from 25.1 to 26.1 σ_θ. It should be also noted that there is a local maximum of the meridional thickness gradient of the 25.1-26.1 σ_θ layer below the eastward current to the west of 160°E around 20°N, which may correspond to the southern STCC (Kobashi et al. 2006).

To study interdecadal variations, we plot the same zonal mean fields for the periods of 1975-79 and 1990-94 (Fig. 6). STCC is stronger and more organized in structure in 25-27^{o}N in the 70s than in the 90s, consistent with Yamanaka et al. (2008). Low-PV water is confined mostly to the STMW density range of 25.2-25.6σ_θ in the 90s but its production increases markedly in the CMW range of 25.5-26.0 σ_θ in the 70s. The low-PV water intrudes much more southward in the 70s than 90s. These changes in low-PV water ventilation are consistent with the STCC change by thermal wind relationship. Our results show that the association between the STCC and PV distribution holds in both the climatology and interdecadal variability in OFES, consistent with observations and the previous study. This encourages us to investigate interannual variations in STCC and its relationship to low-PV water in the next section.

4. Interannual variations in STCC and low-PV water

4-1. Interannual variations in simulated STCC

For investigation of interannual variations in STCC, we plot area-averaged summertime mean zonal velocity at several depths in Fig. 7a. As represented by speed at 54-m depth, STCC has strong interannual variations with a weak mean eastward current. Also, it is clear that the interannual variations are very similar to those at 404-m and 604-m depths. Indeed, vertical profile of correlation with the area-averaged 54-m zonal velocity (Fig. 7c) shows a deep structure, with correlation coefficient, r, higher than 0.9 (0.7) in the upper 600 (1000) m.

Lagged correlation maps (Fig. 8) between 404-m depth summertime zonal current velocity and its area-mean in (26°-28°N, 160°-180°E) indicate that narrow bands of the vertically coherent interannual variations propagate southwestward with a few degrees in meridional width and more than 20° in longitudinal length. These properties resemble those for zonal jets or striations examined by Richards et al. (2006), likely not wind-driven but oceanic internally-induced variability. Indeed, similar lagged correlation maps of Ekman pumping do not show coherent forcing for the zonal current signals indicated in Fig. 8 (figures not shown).

These vertically coherent interannual variations are not related to variations in low-PV water. As the purpose of the present paper is to investigate possible influence of low-PV variations on STCC, in the following analyses, we focus on interannual variations that deviate from the vertically uniform structure. To extract upper layer variations independent of deeper layer variations, we compute the linear regression of the time series of 54-m zonal velocity upon velocity at 404-m depth, and then subtract the regression from the original 54-m zonal velocity time series (Fig. 7b). In the following analyses, we use this new time series averaged in (26°-28°N, 160°-180°E) (Fig. 7b) to represent interannual variations in STCC that is trapped to the near surface layer and independent of the coherent variations in the upper 1000 m. Selection of the depth for the regression, 404 m, is arbitrary, but the resultant time series does not strongly depend on this choice of depth, almost the same results are obtained if regression upon time series at a different depth, say 604-m, is removed. This STCC shear index is a measure of current shear and a good representation of the surface trapped current in climatology.

Simultaneous correlation map between the STCC shear index and summertime 54-m depth zonal velocity (Fig. 9) indicates that the peak of the correlation is about 0.5, and the index explains about 20% of interannual variance in zonal velocity. In other words, major parts of interannual variations in the zonal velocity near the surface are vertically coherent as suggested in Fig. 7. The correlation map shows a dipole pattern with positive and negative correlation zones to the south and north of 27.5°N, respectively, around 160°-180°E, suggesting meridional shift of STCC on interannual time scales.

4-2. Correlation between STCC and low-PV water

To investigate if the STCC interannual variations are related to variations in low-PV water below, we conduct a correlation/regression analysis between the STCC shear index defined above and subsurface fields. Simultaneous correlation maps for PV on a meridional-density section (Fig. 10a) indicate negative correlations appear to the north of STCC around 25.5 to 26.1 σ_θ, while positive correlations are found in shallower layers (shallower than about 25.3 σ_θ). Those negative correlations, representing the intrusion of lower PV water to the north of STCC, are accompanied by a steeper northward shoaling of isopycnals (Fig. 10b, contours). The stronger northward gradient of density corresponds to stronger vertical shear of eastward geostrophic current, consistent with the stronger STCC (shades in Fig. 10b).

Fig. 11 shows lagged correlation maps between the STCC shear index and PV on 25.6 σ_θ isopycnal surface, on which strongest correlations are found in Fig. 10. Negative PV correlations appear at least two years before the peak of STCC, develop and shift south and southwestward. In association with this southwestward shift of negative correlations (which indicate the southwestward development of lower PV water (black contours)), positive correlations of zonal velocity also shift southward and are found to the south of the negative PV correlation region (white contours in Fig. 11), consistent with the meridional shift suggested in Fig. 8. These results strongly suggest that the STCC variations are induced through subduction process of low-PV water that develops more than usual.

The association between STCC and PV anomalies is further examined in a latitude-time section of zonally-averaged (in 160°-180°E) layer thickness in 25.5-26.1 σ_θ layers (Fig. 12). The layer thickness (contours in Fig. 12a) shows significant interannual variations especially in its subduction region (around 32°-36°N), from which the thick layer and its interannual variations extend southward. At the southern edge of a thicker layer, stronger meridional gradients of the thickness (shades in Fig. 12a) induce stronger meridional density gradient and vertical zonal current shear in the upper layer. Indeed, zonal current vertical shear (shades in Fig. 12b) is intensified above the strong meridional gradient of the thickness in 25.5-26.1 σ_θ layers (contours in Fig. 12b), and together they propagate southward coherently. For example, in 26°-28°N, the meridional gradient of the thickness and vertical shear of zonal current, the STCC shear index, has high correlation r=0.77 (Fig. 12c). These results confirm the lagged correlation analysis (Fig. 11).

4-3. Causes of thickness variations

As interannual variations in the thickness of the 25.5-26.1 σ_θ layer can induce interannual variations in STCC, we further investigate what causes the thickness anomalies in the subduction region, which corresponds to 160-180^{o}E, 32-34^{o}N in the climatology. In this subduction region, the interannual variations in the thickness highly correlate with the local SST (r=-0.80) (Fig. 13a), and MLD to the north (34°-36°N) (r=0.65) in the late winter. MLD in the subduction region of 32°-34°N, however, has lower correlation (Fig. 13e), and the correlation between SST and thickness there is not caused by the deepening of the winter mixed layer. To see the relation between SST and thickness variations, we compare latitude-depth sections of wintertime and summertime density between a cold (1995-97) and a warm (2000-02) SST period (Figs. 13b-c). When SST is cold (Fig. 13b), the outcrop line of 25.5 σ_θ layer shifts southward, and the 25.5-26.1 σ_θ layer is exposed to the sea surface in 32°-34°N. Although the 25.5 σ_θ isopycnal surface submerges in summer (blue curve), the 25.5-26.1 σ_θ layer remains thick. In the warm years (Fig. 13c), the outcrop of the 25.5 σ_θ surface shifts northward and the 25.5-26.1 σ_θ layer does not outcrop, is kept thin in winter, and remains thin in summer. SST anomalies in the source region (32°-34°N, 160°-180°E) significantly correlate with eastward wind stress (r=-0.52) and likely influenced by mixing, Ekman cooling, and wind-induced evaporation (but not significantly correlate with the net surface heat flux probably due to cancelation among influences of atmospheric and SST anomalies on the net flux). Additionally, correlation maps of SST and MLD with the thickness in the source region (Figs. 13d-e) indicate that thicker layer tends to be associated with cooler SST anomalies to the south of the Kuroshio Extension Current

(KEC) and deeper MLD near the KEC axis, around which meridional local minimum of MLD forms (Fig. 13e). These anomaly patterns in SST and MLD resemble those with weakened KEC (Nonaka et al., 2011, to be submitted). Indeed, zonally averaged KEC speed (green curve in Fig. 13a) negatively correlates with the thickness (r=-0.64). The relation among variations in KEC, low-PV water subduction, and STCC is suggested by Xie et al. (2011) in their analysis of climate model, and this is supported by the results from this eddy-resolving OGCM hindcast that can represent interannual-to-decadal variations of KEC realistically (Nonaka et al., 2006; Taguchi et al., 2007).

5. Summary and discussion

Based on a 60-year-long hindcast integration of an eddy-resolving OGCM, OFES, we have investigated interannual to decadal variations in STCC and low-PV water and their relations in the North Pacific Ocean. In the model climatology, STCC is found on the south edge of low-PV water as predicted by Kurokawa's (1999) theory and consistent with observations. This close relationship holds for interdecadal variations in STCC and low-PV water in the model. The specific purpose of the present study is to investigate if the relationship between STCC and low-PV water, holds also in interannual variations.

In the OFES hindcast, STCC appears from 150°E to around the international dateline, and is trapped to near the surface. As it peaks in summer near the dateline, we examine interannual variations in summertime STCC and low-PV water. The STCC variability on interannual time scales is dominated by a vertically deep structure (> 1000 m) that seems to relate to narrow bands of zonal currents or striations. We then define an STCC shear by removing vertically coherent variations from variations in the near surface layer zonal velocity, to represent the surface trapped structure of STCC.

A correlation analysis shows that intensified STCC is accompanied by lower PV than usual to the north on 25.5 to 26.1 σ_θ isopycnal surfaces, and by intensified meridional density gradient in subsurface layers (Fig. 10). The low PV signals appear at least two years before peaks of STCC, develop and shift southwestward (Fig. 11). These low-PV signals can be traced back to subduction processes. The results of the correlation analysis are further confirmed by latitude-time sections (Fig. 12).

These results strongly suggest that interannual to decadal variations in STCC are associated with variations of low-PV water ventilation. In other words, the relation between STCC and low-PV water suggested by Kubokawa (1999) and found in the observed climatology (Kobashi et al., 2006) holds in interannual-to-decadal variations at least in this particular model. This mechanism is at work for decadal changes in STCC (Yamanaka et al., 2008), and our study demonstrates that it works also on interannual time scales in addition to the influence of Ekman flow variations shown by Qiu and Chen (2010) and Kobashi and Xie (2011). Sasaki et al. (2011) suggest a similar influence of low-PV water ventilation on interannual variations of HLCC. The Ekman flow influence on STCC is, however, not strong in this model. This may be due to the difference in the region of analyses: the studies of Qiu and Chen (2010) and Kobashi and Xie (2011) focus upon the western northern STCC while the eastern STCC is investigated in this study. Also, weaker meridional temperature gradient in this model than in the observations can weaken the impact of the Ekman flow[1].

Low-PV water distributions in OFES are slightly different from observations as discussed in section 2-2. Indeed, the low-PV waters in the layers around 25.6 σ_θ that correlate with STCC tend to develop and extend more eastward than in observations. This suggests that the relationships between variations in the low-PV water and STCC found in the model may be stronger than in the real ocean. Subsurface observations are still insufficient to investigate this relationship in interannual variations. The accumulation of numerous observations by Argo profilers (Argo Science Team 2001; Hosoda et al., 2010) will make such investigation possible in near future.

Acknowledgments.

The OFES simulations were conducted on the Earth Simulator under the support of JAMSTEC. We thank the members of the OFES group, including Drs. H. Sakuma, Y. Masumoto, and T. Yamagata, for their efforts and supports in the model development. Our thanks are extended to Drs. A. Kubokawa and F. Kobashi for useful discussions. This study is partially supported by Grand-In-Aid for Scientific Research defrayed by the Ministry of Education, Culture, Sports, Science and Technology of Japan (22106006).

[1] Indeed, simulated STF in early spring also show weak correlation (r~0.4 at the maximum) between the Ekman convergence and meridional temperature gradient to about 100-m depth. This is consistent with the result of Qiu and Chen (2010) but the correlation is weaker and spatially incoherent (not shown).

References

Aoki Y, Suga T, Hanawa K (2002) Subsurface subtropical fronts of the North Pacific as inherent boundaries in the ventilated thermocline. J. Phys. Oceanogr., 32, 2299-2311.

Argo Science Team (2001) Argo: The global array of profiling floats. In: CJ Koblinsky and NR Smith, (eds) Observing the Oceans in the 21st Century, GODAE Project Office, Bureau of Meteorology, Melbourne, pp. 248-258.

Hanawa K, Talley L (2001) Mode waters, in Ocean Circulation and Climate, Int. Geophys. Ser., edited by G. Siedler, J. Church, and J. Gould, pp. 373-386, Elsevier, New York.

Hosoda S, Ohira T, Sato K, Suga T (2010) Improved description of global mixed-layer depth using Argo profiling floats. J. Oceanogr., 66, 773-787.

Inui T, Takeuchi K, Hanawa K (1999) A Numerical Investigation of the Subduction Process in Response to an Abrupt Intensification of the Westerlies. J. Phys. Oceanogr., 29, 1993–2015.

Kalnay E et al. (1996) The NCEP/NCAR 40-year reanalysis project. Bull. Amer. Meteor. Soc., 77, 437-471.

Kobashi F, Kawamura H (2001) Variation of sea surface height at periods of 65-220 days in the subtropical gyre of the North Pacific. J. Geophys. Res., 106, 26,817-26,831.

Kobashi F, Kawamura H (2002) Seasonal variation and instability nature of the North Pacific Subtropical Countercurrent and the Hawaiian Lee Countercurrent. J. Geophys. Res., 107, 3185, doi:10.1029/2001JC001225.

Kobashi F, Mitsudera H, Xie SP (2006) Three subtropical fronts in the North Pacific: Observational evidence for mode water-induced subsurface frontogenesis. J. Geophys. Res., 111, C09033, doi:10.1029/2006JC003479.

Kobashi F, Xie SP, Iwasaka N, Sakamoto T (2008) Deep atmospheric response to the North Pacific oceanic subtropical front in spring. J. Climate, 21, 5960-5975.

Kobashi F, Xie SP (2011) Interannual variability of the North Pacific Subtropical Countercurrent: Role of local ocean-atmosphere interaction. J. Oceanogr., submitted.

Kubokawa A (1999) Ventilated thermocline strongly affected by a deep mixed layer: A theory for subtropical countercurrent. J. Phys. Oceanogr., 29, 1314-1333.

Kubokawa A, Inui T (1999) Subtropical countercurrent in an idealized ocean GCM. J. Phys. Oceanogr., 29, 1303-1313.

Large WG, McWilliams JC, Doney SC (1994) Oceanic vertical mixing: A review and a model with a nonlocal boundary layer parameterization. Rev. Geophys., 32, 363-403.

Masumoto Y, Sasaki H, Kagimoto T, Komori N, Ishida A, Sasai Y, Miyama T, Motoi T, Mitsudera H, Takahashi K, Sakuma H, Yamagata T (2004) A Fifty-Year Eddy-Resolving Simulation of the World Ocean -Preliminary Outcomes of OFES (OGCM for the Earth Simulator)-, J. Earth Simulator, 1, 31-52.

Masuzawa J (1969) Subtropical mode water, Deep Sea Res., 16, 436-472.

Nakamura H (1996) A pycnostad on the bottom of the ventilated portion in the central subtropical North Pacific: Its distribution and formation. J. Oceanogr., 52, 171-188.

Nonaka M, Nakamura H, Tanimoto T, Kagimoto T, Sasaki H (2006) Decadal variability in the Kuroshio-Oyashio Extension simulated in an eddy-resolving OGCM. J. Climate, 19, 1970–1989.

Nonaka M, Nakamura H, Tanimoto Y, Kagimoto T, Sasaki H (2008) Interannual-to-decadal variability in the Oyashio Current and its influence on temperature in the subarctic frontal zone: An eddy-resolving OGCM simulation. J. Climate, 21, 6283-6303.

Oka E, Suga T (2006) Differential formation and circulation of North Pacific central mode water. J. Phys. Oceanogr., 35, 1997-2011.

Pacanowski RC, Griffies SM (2000) MOM 3.0 Manual. Geophysical Fluid Dynamics Laboratory/National Oceanic and Atmospheric Administration, 680pp.

Qiu B, Koh DA, Lumpkin C, Flament P (1997) Existence and Formation Mechanism of the North Hawaiian Ridge Current. J. Phys. Oceanogr., 27, 431–444.

Qiu B (1999) Seasonal eddy field modulation of the North Pacific subtopical countercurrent: TOPEX/Poseidon observations and theory. J. Phys. Oceanogr., 29, 2471-2486.

Qiu B, Chen S (2010) Interannual variability of the North Pacific subtropical countercurrent and its associated mesoscale eddy field. J. Phys. Oceanogr., 40, 213-225.

Richards KJ, Maximenko NA, Bryan FO, Sasaki H (2006) Zonal jets in the Pacific Ocean. Geophys. Res. Lett., 33, L03605, doi:10.1029/2005GL024645.

Roden GI (1975) On the North Pacific temperature, salinity, sound velocity fronts, and the relation to the wind and energy flux fields. J. Phys. Oceanogr., 5, 557-571.

Sasaki H, Nonaka M, Masumoto Y, Sasai Y, Uehara H, Sakuma H (2007) An eddy-resolving hindcast simulation of the quasi-global ocean from 1950 to 2003 on the Earth Simulator. In: K Hamilton and W Ohfuchi, (eds) High resolution numerical modelling of the atmosphere and ocean, Springer, New York, pp. 157-185.

Sasaki H, Xie SP, Taguchi B, Nonaka M, Hosoda S, Masumoto Y (2011) Interannual variations of the Hawaiian Lee Countercurrent induced by low potential vorticity water ventilation in the subsurface, J. Oceanogr., submitted.

Smith RD, Maltrud ME, Bryan FO, Hecht MW (2000) Numerical simulation of the North Atlantic Ocean at 1/10°. J. Phys. Oceanogr., 30, 1532-1561.

Suga T, Takei Y, Hanawa K (1997) Thermostad distribution in the North Pacific subtropical gyre: The central mode water and the subtropical mode water. J. Phys. Oceanogr., 27, 140-152.

Suga T, Motoki K, Aoki Y, Macdonald AM (2004) The North Pacific climatology of winter mixed layer and mode waters. J. Phys. Oceanogr., 34, 3-22.

Taguchi B, Xie SP, Schneider N, Nonaka M, Sasaki H, Sasai Y (2007) Decadal variability of the Kuroshio Extension: Observations and an eddy-resolving model hindcast. J. Climate, 20, 2357-2377.

Taguchi B, Qiu B, Nonaka M, Sasaki H, Xie SP, Schneider N (2010) Decadal Variability in the Kuroshio Extension: Mesoscale Eddies and Recirculations. Ocean Dynamics, 60, 673-691. DOI 10.1007/s10236-010-0295-1

Takeuchi K (1984) Numerical study of the subtropical front and the subtropical countercurrent. J. Oceanogr. Soc. Jpn., 40, 371-381.

Uda M, Hasunuma K (1969) The eastward subtropical countercurrent in the western North Pacific Ocean. J. Oceanogr. Soc. Jpn., 25, 201-210.

White WB, Hasunuma K, Solomon H (1978) Large scale seasonal and secular variability of the Subtropical Front in the Western North Pacific from 1954 to 1974. J. Geophys. Res., 83, 4531-4544.

Xie SP, Kunitani T, Kubokawa A, Nonaka M, Hosoda S (2000) Interdecadal thermocline variability in the North Pacific for 1958-97: A GCM simulation. J. Phys. Oceanogr., 30, 2798-2813.

Xie SP, Liu T, Liu Q, Nonaka M (2001) Far-reaching effects of the Hawaiian Islands on the Pacific Ocean-atmosphere. Science, 292, 2057-2060.

Xie SP, Deser C, Vecchi GA, Ma J, Teng H, Wittenberg AT (2010) Global warming pattern formation: Sea surface temperature and rainfall. J. Climate, 23, 966-986.

Xie SP, Xu L, Liu Q, Kobashi F (2011) Dynamical role of mode water ventilation in decadal variability in the central subtropical gyre of the North Pacific. J. Climate, in press.

Yamanaka G, Ishizaki H, Hirabara M, Ishikawa I (2008) Decadal variability of the subtropical front of the western North Pacific in an eddy-resolving ocean general circulation model. J. Geophys. Res., 113, C12027, doi:10.1029/2008JC005002.

Yoshida K, Kidokoro T (1967) A subtropical countercurrent in the North Pacific—An eastward flow near the subtropical convergence. J. Ocenaogr. Soc. Jpn., 23, 88-91.

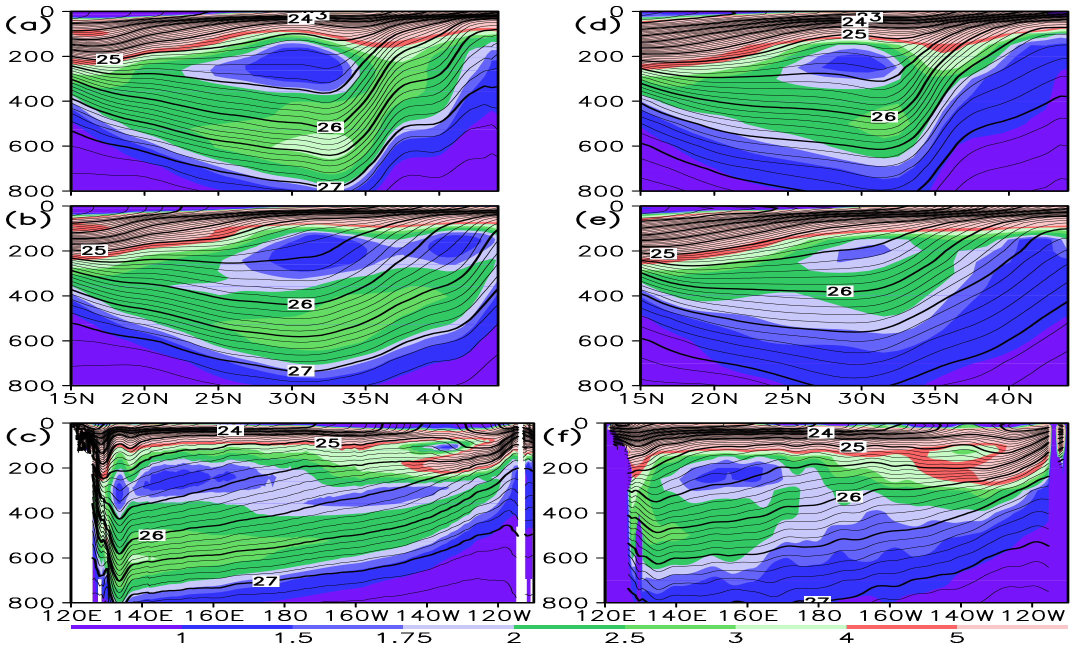

Figure 1. Potential vorticity (shades as indicated at the bottom of panels in 10^{-12} cm^{-1} sec^{-1}) and density (contours, with intervals of 0.1 σ_θ) distributions in OFES (a, b, c) and observational data (d, e, f). (a, d) Latitude-depth section of 145˚-155˚E mean. (b, e) The same as (a, d), but for 165˚-175˚E mean. (c, f) Longitude-depth section of 27˚-29˚N mean.

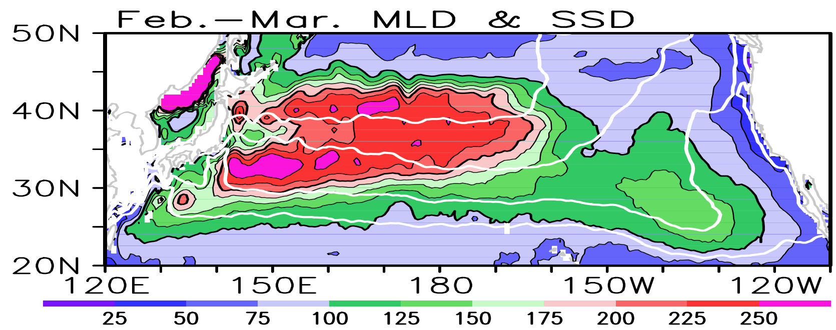

Figure 2. Long-term mean late winter (February-March) mixed layer depth (MLD; shades in m) and sea surface density (white contours for 24.5, 25.0, 25.5, and 26.0 σ_θ) fields simulated in OFES. The color scale is given at the bottom of the panel. MLD is defined as the depth where density difference from the sea surface exceeds 0.125 σ_θ.

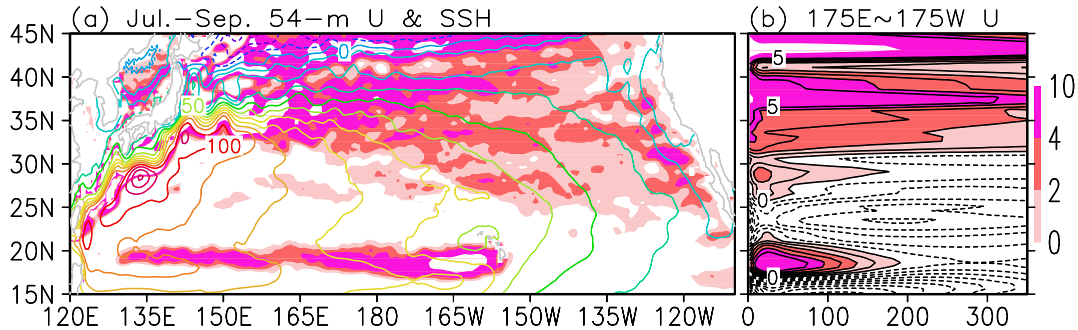

Figure 3. Long-term mean summertime (July-September) zonal current velocity (shades as indicated to the right of panel (b) in cm sec^{-1}) (a) at 54-m depth and (b) in 175˚E-175˚W mean latitude-depth section in OFES. Contours in (a) is the corresponding sea surface height field (contour intervals are 10 cm).

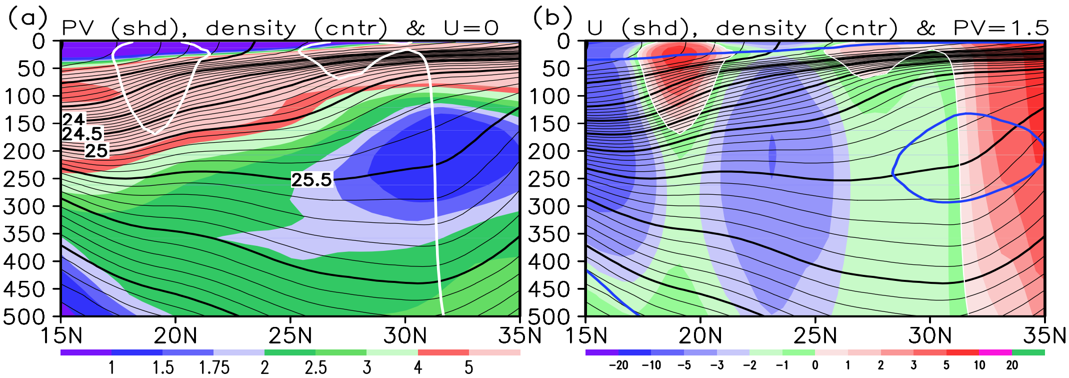

Figure 4. Latitude-depth sections of summertime (July-September) (a) potential vorticity (shades), (b) zonal velocity (shades), and density (black contours in panels a and b; intervals are 0.1 σ_θ). All variables are based on OFES simulation, and are long-term mean and zonally averaged in 160˚-180˚E. White (blue) contours in panel a (b) are for zonal velocity of 0 cm sec^{-1} (potential vorticity of 1.5 10^{-12} cm^{-1} sec^{-1}). Shades are indicated as shown at the bottom of each panel.

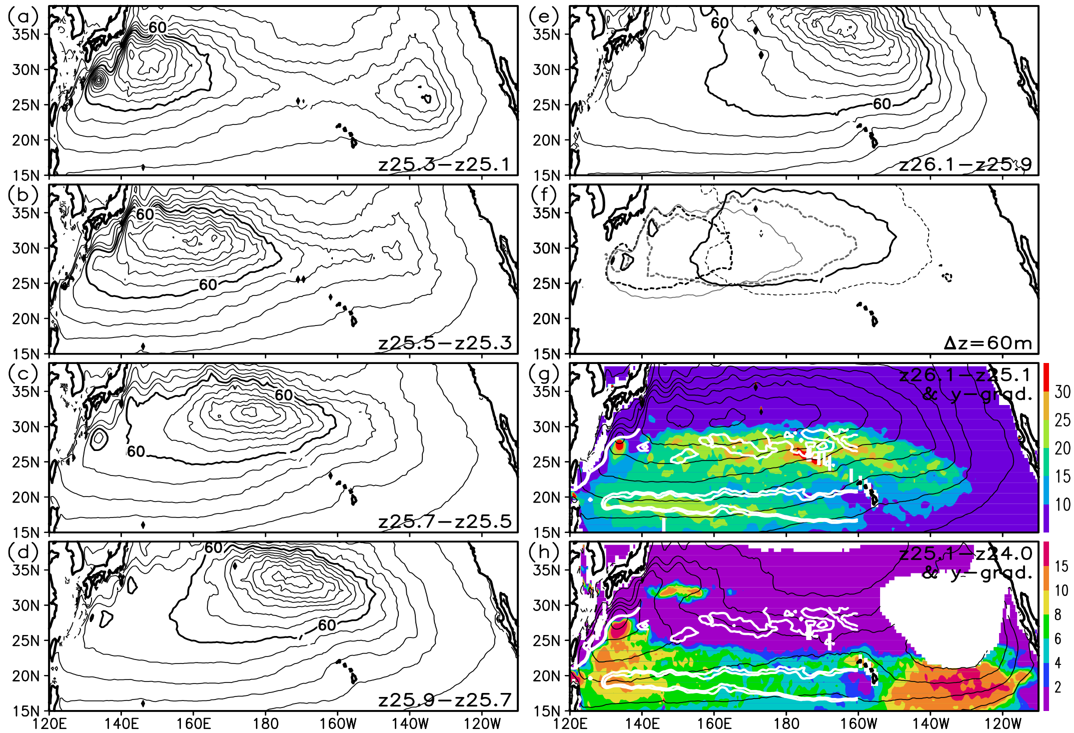

Figure 5. Horizontal distributions of summertime (July-September) layer thickness for (a) 25.1-25.3 σ_θ, (b) 25.3-25.5 σ_θ, (c) 25.5-25.7 σ_θ, (d) 25.7-25.9 σ_θ, (e) 25.9-26.1 σ_θ, (g) 25.1-26.1 σ_θ, and (h) 24.0-25.1 σ_θ. (f) The same as (a) but for thickness = 60 m for each layer in panels (a-e). Shades in panels (g-h) show meridional gradient of the corresponding thickness (m latitude^{-1}), and white contours show zonal velocity = 0, and 2 cm sec^{-1} at 54-m depth. All are the long-term mean simulated fields.

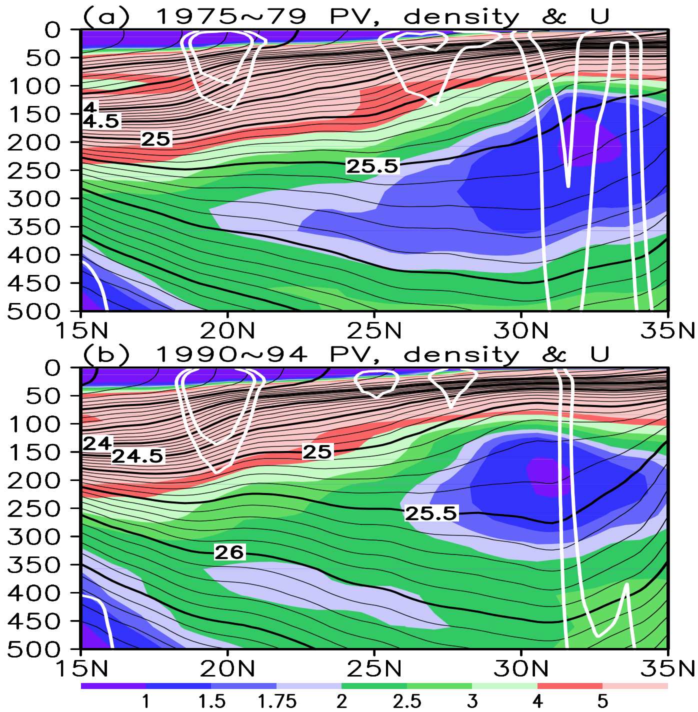

Figure 6. The same as Fig. 4a, but for the fields averaged in summer time in (a) 1975-1979 and (b) 1990-1994. White contours for the zonal current field show 0 and 2 cm sec^{-1}.

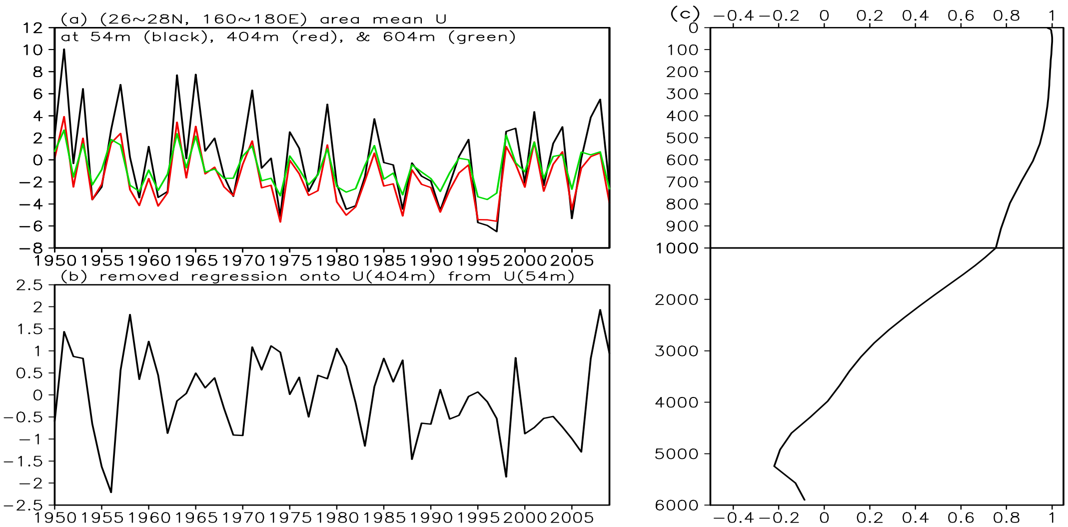

Figure 7. (a) Time series of area mean simulated summertime (July-September) zonal current velocity in (26˚-28˚N, 160˚-180˚E) at 54-m (black), 404-m (red), and 604-m (green) depths. (b) Time series of the index of STCC vertical shear that is defined in the text. (c) Vertical profile of correlation coefficients between the area mean simulated zonal current velocity in (26˚-28˚N, 160˚-180˚E) at 54-m depth and those at each vertical level.

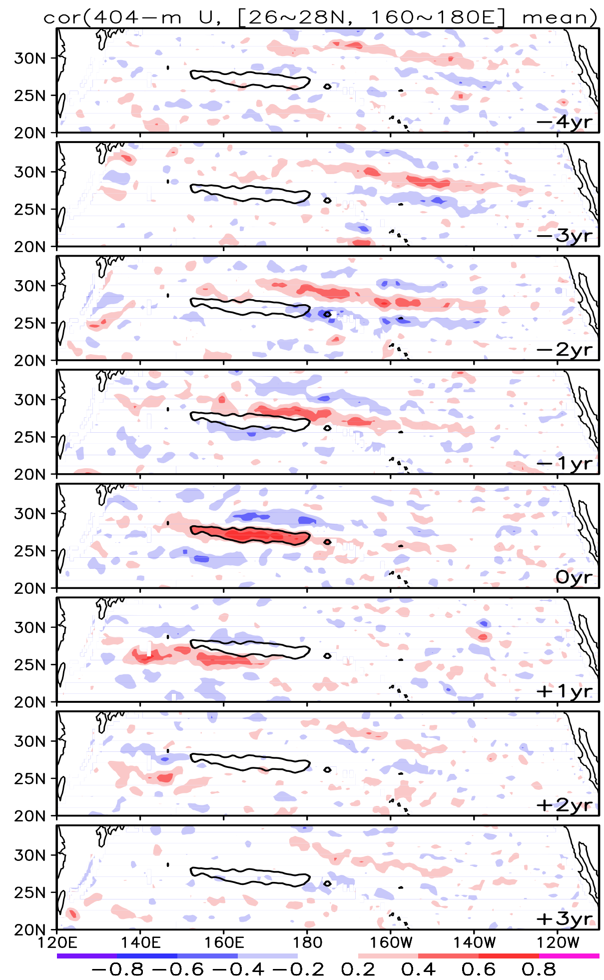

Figure 8. Lagged correlation (shades) maps of summertime (July-September) simulated 404-m depth zonal current onto the same field averaged in (26˚-28˚N, 160˚-180˚E) with lags of -4 to +3 years from the top to bottom. Black contours show the simultaneous correlation = 0.4.

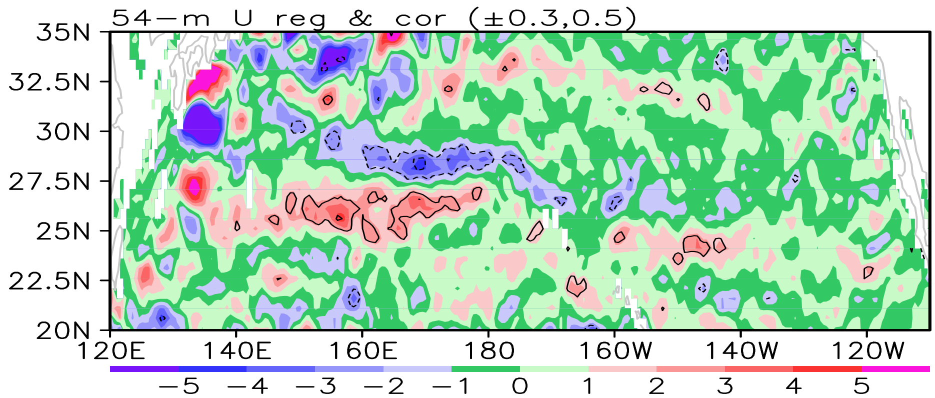

Figure 9. Simultaneous correlation (contours for +/- 0.3, 0.5) and regression (shades as indicated at the bottom of the panel) coefficients between summertime (July-September) 54-m depth zonal current velocity and the STCC shear index (Fig. 7b).

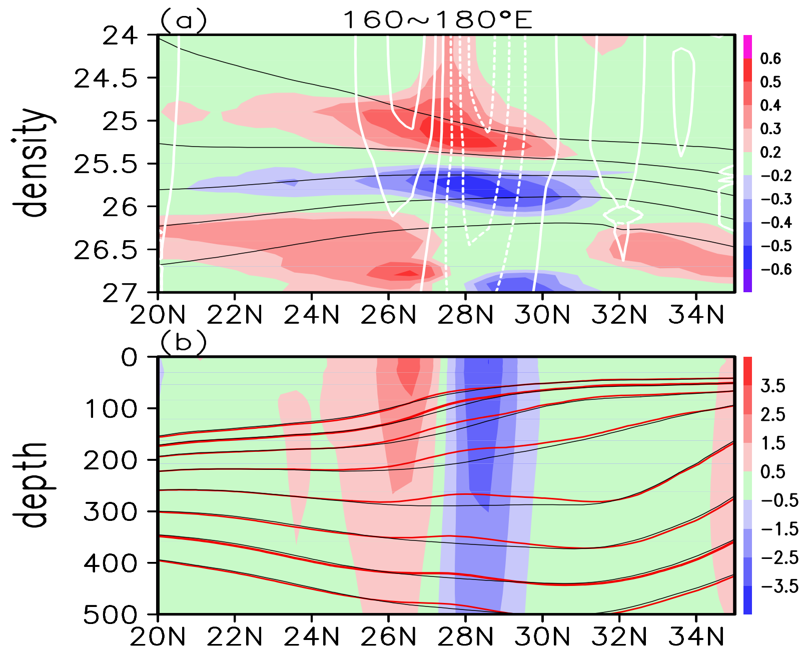

Figure 10. (a) Correlation of 160˚-180˚E mean PV (shades) and regression map of 160˚-180˚E mean zonal velocity (white contours with 1 cm sec^{-1} intervals) onto the STCC shear index as a function of latitude and density. (b) The same as the top panel, but for the meridional-depth regression maps for zonal velocity (shades) and density (red contours with climatology added). The regression maps correspond to 1 cm sec^{-1} anomaly of the STCC index. Black contours in (a) and (b) are long-term mean isopycnal depth (100 to 500 m, with 100-m intervals) and density (24.8 to 26.2, with 0.2 σ_θ intervals). All variables are summertime (July-September) simulated fields.

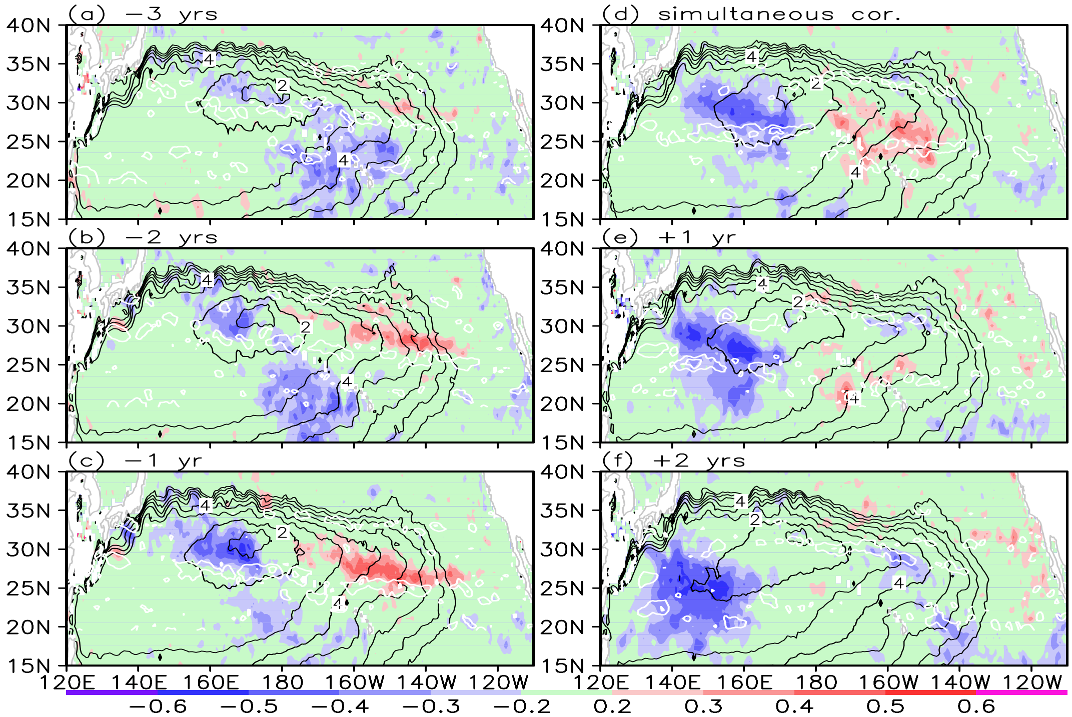

Figure 11. Lagged correlation (shades) and regression (black contours) maps of PV on 25.6 σ_θ surface onto the STCC shear index with lags of (a) -3, (b) -2, (c) -1, (d) 0, (e) 1, and (f) 2 years. White contours show the corresponding correlation (0.2, and 0.4) map of 54-m depth zonal velocity onto the STCC shear index. The regression maps correspond to 1 cm sec^{-1} anomaly of the index with climatology added. All variables are summertime (July-September) simulated fields.

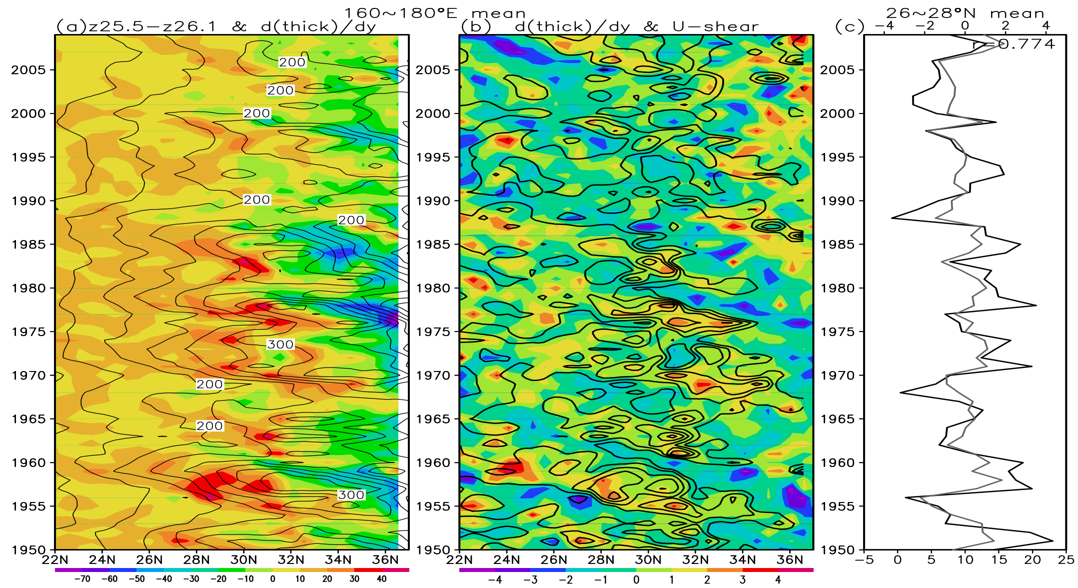

Figure 12. (a) Latitude-time section of 25.5-26.1 σ_θ layer thickness (contours; intervals are 25 m) and its meridional gradient (shades; in m latitude^{-1}). (b) The same as (a), but for vertical shear of zonal velocity (shades). Contours are the same field as that shown in shades in (a). (c) 26˚-28˚N mean vertical shear of zonal velocity (black, top axis), which is identical to the STCC shear index (Fig. 7b), and meridional gradient of thickness shown in (a, b) (grey, bottom axis). All variables are 160˚-180˚E mean of summertime (July-September) simulated fields. The vertical shear in (b) is defined in the same way as the STCC shear index (Fig. 7b).

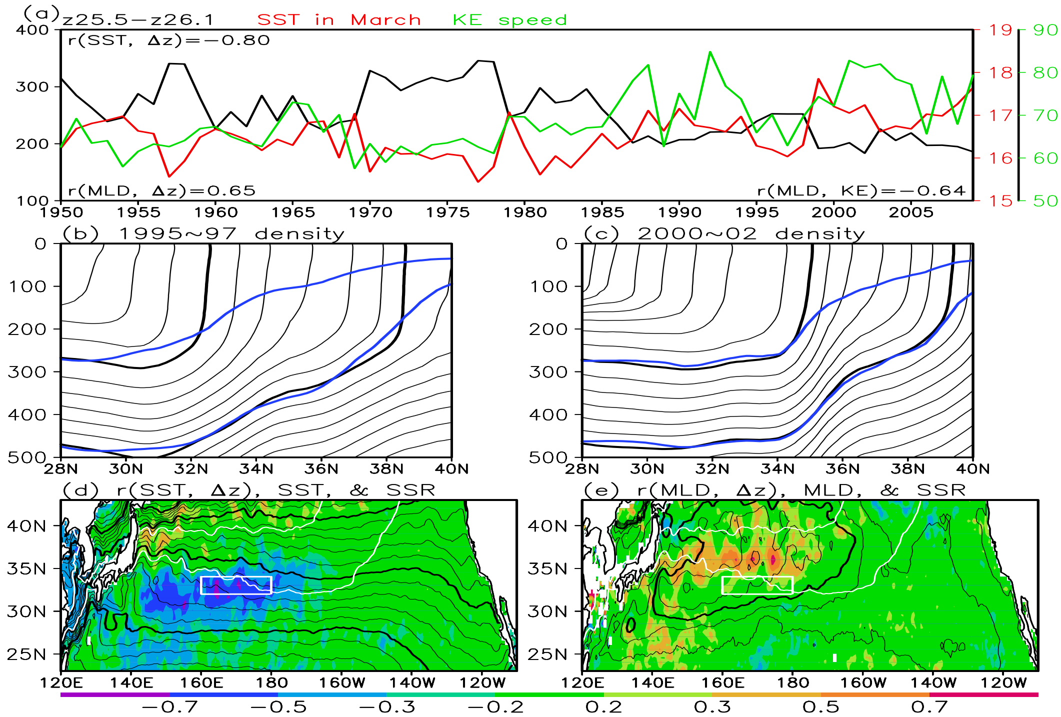

Figure 13. (a) Time series of 25.5-26.1 σ_θ layer thickness (black; left axis) in summertime (July-September), SST (red; right axis) in March both averaged in (32˚-34˚N, 160˚-180˚E), and the surface Kuroshio Extension Current speed (green; right most axis in cm sec^{-1}) in March averaged in 140˚-180˚E. The Kuroshio Extension Current speed is detected at each zonal grid point as a maximum zonal current speed in 30˚-40˚N. (b-c) Meridional-depth sections of 160˚-180˚E mean density in March (black contours with 0.1 σ_θ intervals and thickened for 25.5 and 26.1 σ_θ), and in summertime (blue for 25.5 and 26.1 σ_θ). (b) is for the average fields in 1995-97, and (c) is for those in 2000-2002. (d-e) Correlation map of SST (d) and MLD (e) in March onto the time series of layer thickness shown in panel (a). Black contours indicate the long-year mean of the corresponding field, and white contours show sea surface density (25.5 and 26.1 σ_θ). All variables are simulated fields.